Electronic Supplementary Material (ESI) for Journal of Materials Chemistry A.
This journal is © The Royal Society of Chemistry 2021

SUPPLEMENTARY INFORMATION

Face-On Oriented Hydrophobic Conjugated Polymers as Dopant-Free Hole-Transport Materials for Efficient and Stable Perovskite Solar Cells with Fill Factor Approaching 85%

Lusheng Liang,[a,b] Naoyuki Shibayama,[c] Haiying Jiang,[d] Zilong Zhang,[a,b] Lingyi Meng,[a,b] Lianjie Zhang,[d] Can Wang,[a,b] Nan Zhao,[e] Yaming Yu,[e] Seigo Ito,[f] Jihuai Wu,[e] Junwu Chen*[d] and Peng Gao*[a,b]*

[a.] CAS Key Laboratory of Design and Assembly of Functional Nanostructures, and Fujian Provincial Key Laboratory of Nanomaterials Fujian Institute of Research on the Structure of Matter, Chinese Academy of Sciences, Fuzhou, Fujian 350002, China

[b.] Laboratory for Advanced Functional Materials, Xiamen Institute of Rare Earth Materials, Haixi Institute, Chinese Academy of Sciences, and Xiamen Key Laboratory of Rare Earth Photoelectric Functional Materials, Xiamen 361021, China

[c.] Faculty of Biomedical Engineering, Graduate School of Engineering, Toin University of Yokohama, 1614 Kurogane-cho, Aoba, Yokohama, Kanagawa 225-8503, Japan

[d.] Institute of Polymer Optoelectronic Materials and Devices, State Key Laboratory of Luminescent Materials and Devices, South China University of Technology, Guangzhou 510640, People's Republic of China

[e.] College of Materials Science and Engineering, Huaqiao University, 361021 Xiamen, China

[f.] Department of Materials and Synchrotron Radiation Engineering, Graduate School of Engineering, University of Hyogo, Himeji 671-2280, Japan

* E-mail: lianjiezhang@scut.edu.cn; psjwchen@scut.edu.cn; peng.gao@fjirsm.ac.cn

1. Experimental

1.1 Device fabrication and characterization

Materials: SnO_2 colloid precursor (tin (IV) oxide, 15% in H_2O colloidal dispersion) was purchased from Alfa Aesar. Lead iodide (99.99%) was purchased from TCI, lead bromide (99.999%) and cesium iodide (99.9%) were bought from Sigma-Aldrich. Formamidinium iodide (FAI) and methylammonium bromide (MABr) were synthesized by reacting

formamidine acetate (Aladdin) and hydroiodic acid (55.0-58.0 wt% in H_2O, Aladdin), methylamine (30-33 wt% in ethanol, Aladdin) and hydrobromic acid (48 wt% in H_2O, Aladdin), respectively. The particular experimental operations were referred to as previously reported methods.[1] spiro-OMeTAD was purchased from Derthon Optoelectronic Materials Science Technology Co LTD.

Fabrication of the devices: The ITO substrate was washed with deionized water, acetone, and anhydrous ethanol for 15 min, respectively. Then, after the dry clean substrates were treated by plasma for 10 min, a thin layer of SnO_2 nanoparticle film (SnO_2 colloid precursor diluted by deionized water, 1: 3, weight ratio) were spin-coated on the ITO substrates at 3000 rpm for 30 s and annealed in ambient air at 150 °C for 30 min. Next, a CsFAMA triple-cation "mixed" perovskite precursor solution was prepared by dissolving PbI_2 (1.2 M), FAI (1.1 M), $PbBr_2$ (0.2 M) and MABr (0.2 M) in a mixed solvent of anhydrous DMF and DMSO (4:1, volume ratio). After stirring for 30 min, 60 μL CsI which was previously dissolved as a 1.5 M stock solution in DMSO was added to the mixed perovskite precursor solution. Then, the perovskite precursor solution was spin-coated onto the substrates with SnO_2 via using a two steps procedure (the first step is under 1000 rpm for 10 s and the second step is under 6000 rpm for 30 s) in a nitrogen glove box. When entering the last 5 seconds before the second step finish, the anti-solvent (150 μL of chlorobenzene) were dropped on the spinning substrate.[2] The substrates were then annealed on a hotplate at 100 °C for 30 min. Afterwards, the substrates were cooled to room temperature, and the solution with different HTMs were spin-coated on different substrates containing perovskite layers. For spiro-OMeTAD solution, 72.3 mg of spiro-OMeTAD was dissolved 1 mL of chlorobenzene with additives of 17.5 μL of bis(trifluoromethylsulfonyl)imide lithium salt (Li-TFSI, Sigma-Aldrich) solution (520 mg mL^{-1} in acetonitrile), 28.5 μL of 4-tert-butylpyridine (TBP, Sigma-Aldrich), the spin-coating condition: 4000 rpm for 30 s. For HTMs of PBZ-1Si, PBZ-2Si and PBZ-3Si, the optimized 4 mg mL^{-1}, 6 mg mL^{-1} and 6 mg mL^{-1} were prepared in chlorobenzene, respectively, the spin-

coating condition: 2500 rpm for 30 s. Finally, 80 nm of the gold counter electrode was thermally evaporated under high vacuum.

Film and device characterization: The grazing incident wide-angle X-ray scattering (GIWAXS) measurements were performed at BL46XU beamline of SPring-8. PBZ-3Si and spiro-OMeTAD samples were prepared on Si substrates or the surface of ITO/SnO_2/perovskite film. The sample was irradiated with an X-ray energy of 12.39 keV (λ = 1 Å) at a fixed-incident angle on the order of 0.12° through a Huber diffractometer. The GIWAXS pattern was recorded with a two-dimensional image detector (Pilatus 300 K). The surface morphology was characterized by scanning electron microscopy (SEM) and atomic force microscopy (AFM). The cross-sectional view morphology of the perovskite films was observed using a field-emission scanning electron microscope (SEM, Apreo S). The roughness of the films was recorded using atomic force microscopy (AFM, Multimode-8J, America). Contact angles were characterized on an Optical contact angle measuring and contour analysis systems (OCA40 Micro). Photoluminescence was measured at room temperature on a fluorescence spectrophotometer (FLS980, Edinburgh Instruments). The steady-state PL emissions were measured under 700 nm light source excitation using monochromatized Xe lamp, while the time-resolved PL decays were carried out with a pulsed diode laser excitation source. The X-ray photoelectron spectrum (XPS) was performed using an X-ray photoelectron spectroscopy system (Axis Supra, Shimadzu) with Al Kα X-ray radiation (1486.6 eV) as the X-ray source, and C-C (C1s) peak at 284.8eV is used as a charge correction reference. The photovoltaic performance of devices was measured with a Keithley 2401 source meter using a solar simulator (SS-F5-3A, Enlitech) at 100 mW cm^{-2} illumination (AM 1.5 G) equipped with a calibrated Si reference cell (SRC-2020, Enlitech). The J–V curves of the PSCs were measured in reverse scan (from 1.2 to -0.1 V) or forward scan (from -0.1 to 1.2 V) modes at a scan speed of 200 mV s^{-1}. The active area of devices was defined by a metal shadow mask of 0.1 cm^2. External quantum effciency (EQE) was obtained on a computer-controlled quantum efficiency

measuring instrument (QE-R, Enlitech). Electrochemical impedance spectroscopy (EIS) measurements were carried out under 10 mW cm^{-2} illumination at applied voltages (-0.85 V) using an electrochemical workstation (Zennium Zahner, Germany) with an AC perturbation of 10 mV ranging from 100 mHz to 1 MHz, at room temperature with 40-50% humidity. Transient photocurrent decay (TPC) was performed at short circuit condition under white light bias generated from an array of light-emitting diodes equal to 1 sun intensity. Transient photovoltage (TPV) measurements was performed at open circuit condition under white light bias generated from an array of light-emitting diodes equal to 1 sun intensity. Stability test: The dark long-term stability assessment of the perovskite solar cells was carried out by repeating the *J-V* characterizations over various times. The unsealed devices were stored under ambient atmosphere with 20 ± 5% relative humidity at room temperature. The high thermal and humidity long-term stability was carried out (devices without encapsulation) on a hot plate at the temperature of 85 °C under 70 ± 10% RH ambient atmosphere. Space-charge-limited current (SCLC) measurement based on the hole-only devices (ITO/PEDOT:PSS/HTM/MoO_3/Ag); the dark J-V characteristics of the devices were measured by a Keithley 2401 source meter in the range of 0-5 V. The hole mobility (μ) can be extracted from the trap-free SCLC regime, according to Mott-Gurney law:

$$J_D = \frac{9\mu\varepsilon_r\varepsilon_0 V_b^2}{8L^3} \qquad \text{(S1)}$$

Where J_D is the current density, V_b is applied voltage, L is the thickness of HTM film, ε_r is the relative dielectric constant of organic materials (ε_r=3), ε_0 is the vacuum permittivity, and q is the electron charge.[3]

1.2 DFT calculation

The ground-state geometry optimization was calculated using density functional theory (DFT) method at the B3LYP/6-31G(d) level of theory with the Gaussian 09 program package.[4] Stationary points were verified by frequency analysis. The optimized structures were found to

be stable. The calculated molecular electronic static potential (ESP) results were obtained with the Multiwfn 3.7 program.[5]

2. Additional Figures and Data

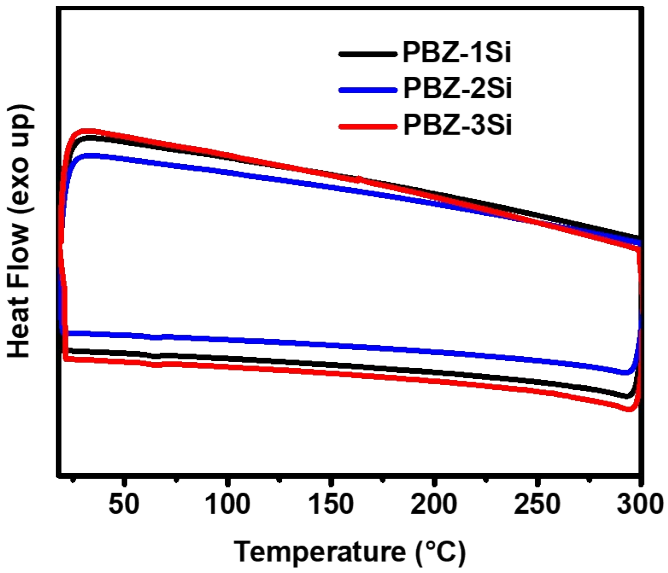

Figure S1. Differential scanning calorimetry curves during the second heating scan for PBZ-Si.

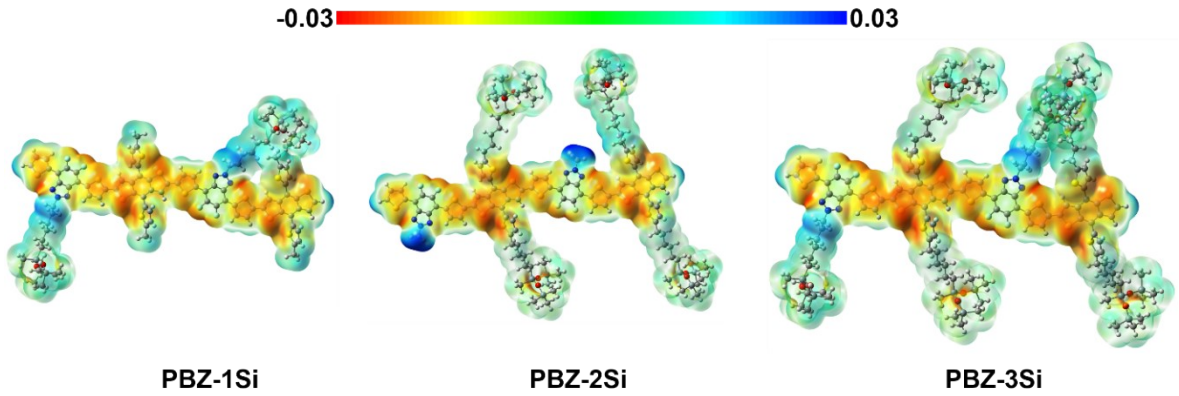

Figure S2. Calculated ESP profiles of PBZ-Si polymers.

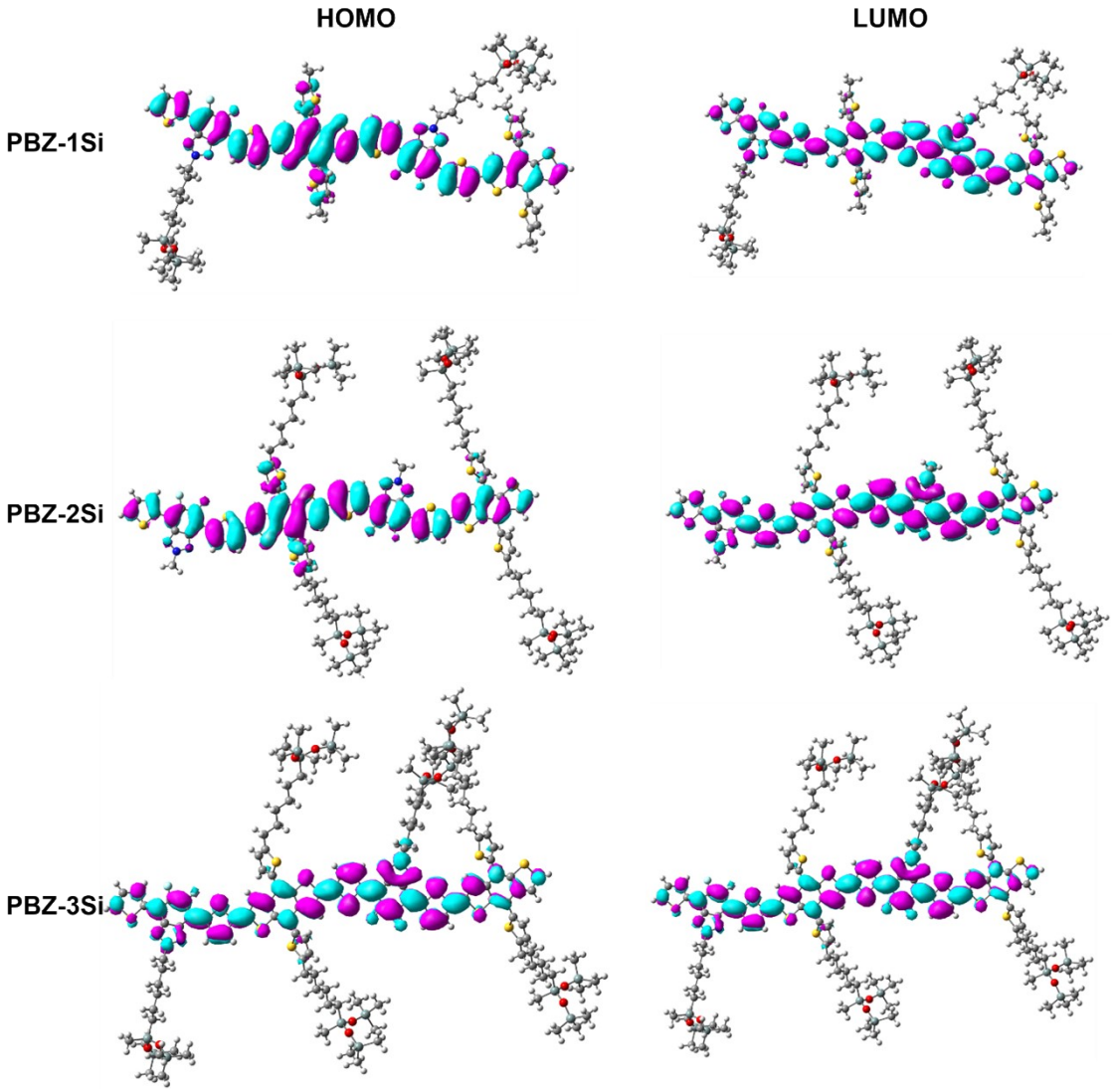

Figure S3. HOMO and LUMO of PBZ-Si polymers obtained from DFT calculations.

Table S1. Calculated HOMO and LUMO energy levels of polymers.

Samples	HOMO (eV)	LUMO (eV)
PBZ-1Si	–4.74	–2.40
PBZ-2Si	–4.74	–2.42
PBZ-3Si	–4.71	–2.38

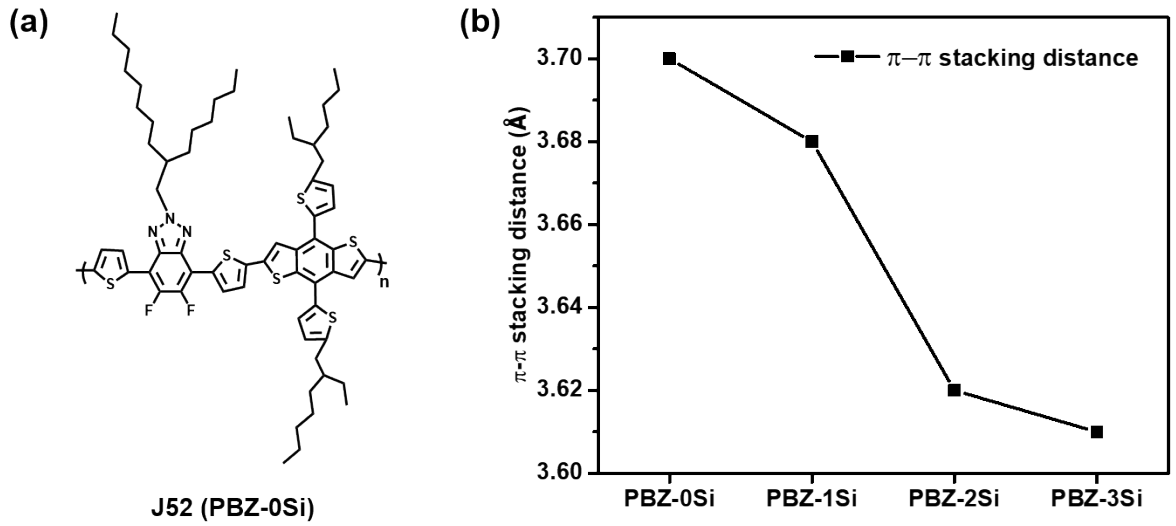

Figure S4. (a) The structure of J52 molecular[6] which represents the PBZ-0Si. (b) π–π distance of polymers.

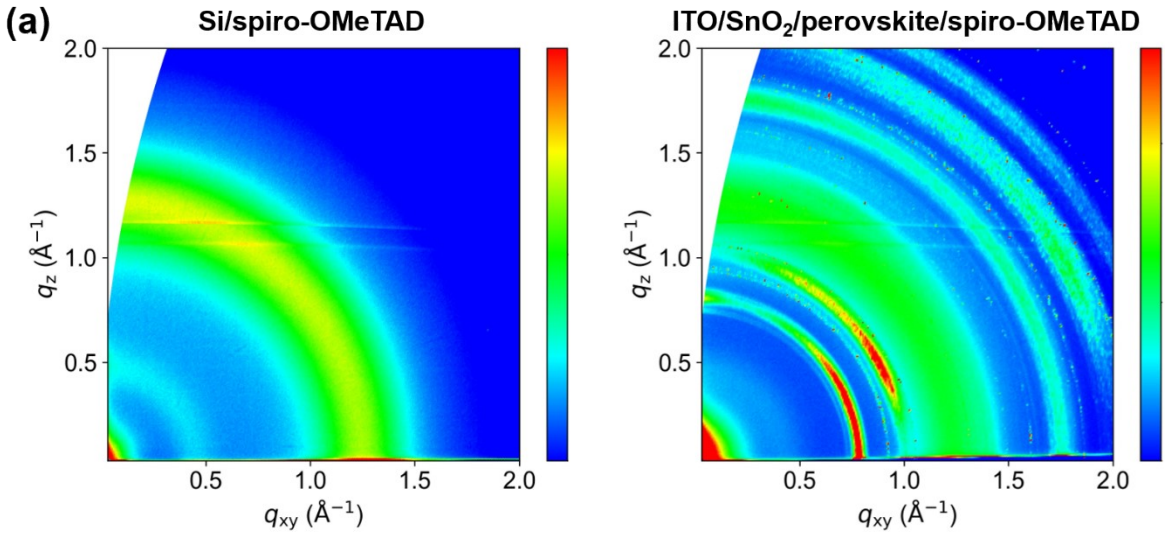

Figure S5. GIWAXS patterns of the spiro-OMeTAD films coated on different substrates: (a) Si/spiro-OMeTAD, and (b) ITO/SnO_2/perovskite/spiro-OMeTAD.

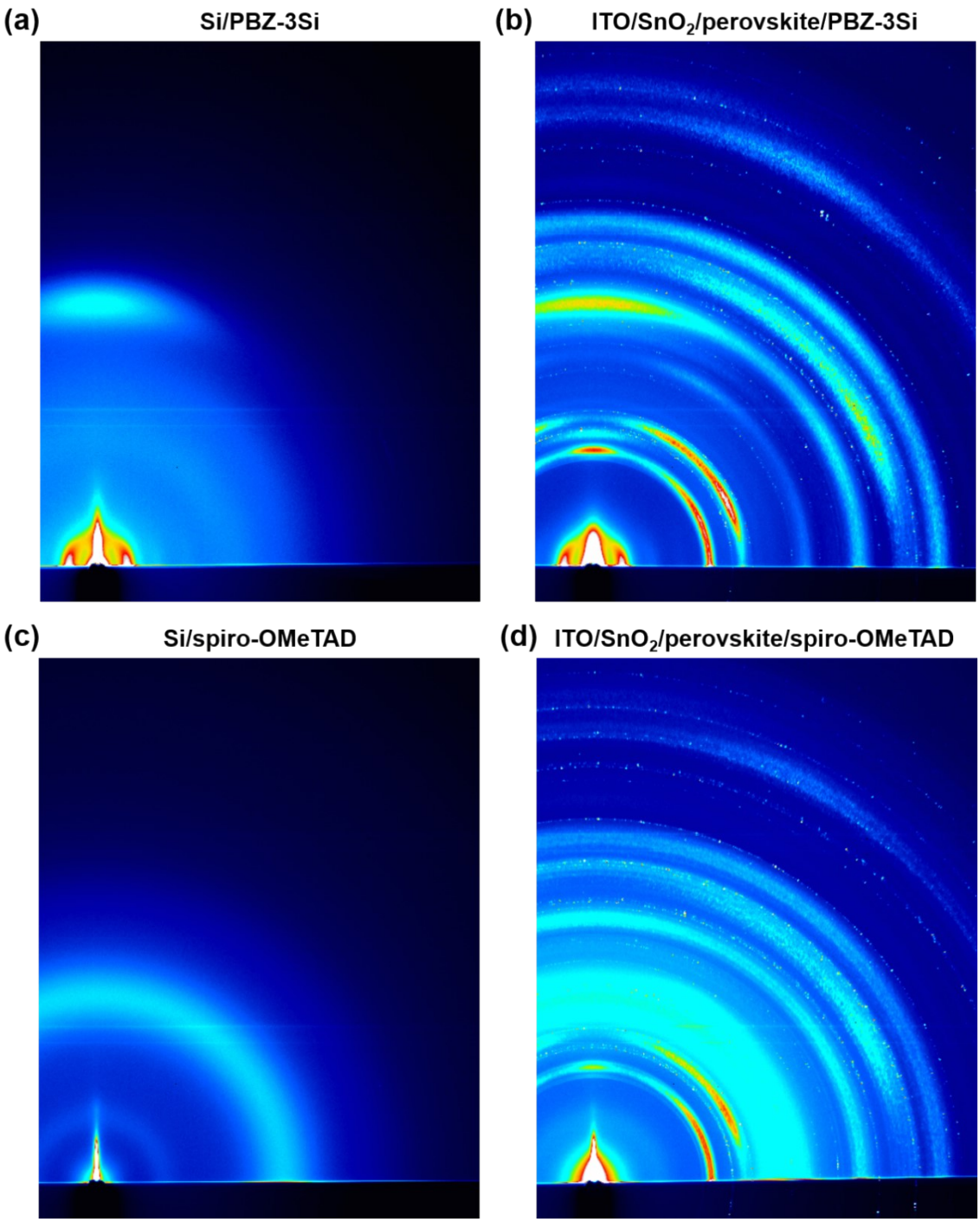

Figure S6. Image data of 2D X-ray detector for GIWAXS measurements (a) Si/PBZ-3Si, (b) ITO/SnO_2/perovskite/PBZ-3Si, (c) Si/spiro-OMeTAD, and (d) ITO/SnO_2/perovskite/spiro-OMeTAD.

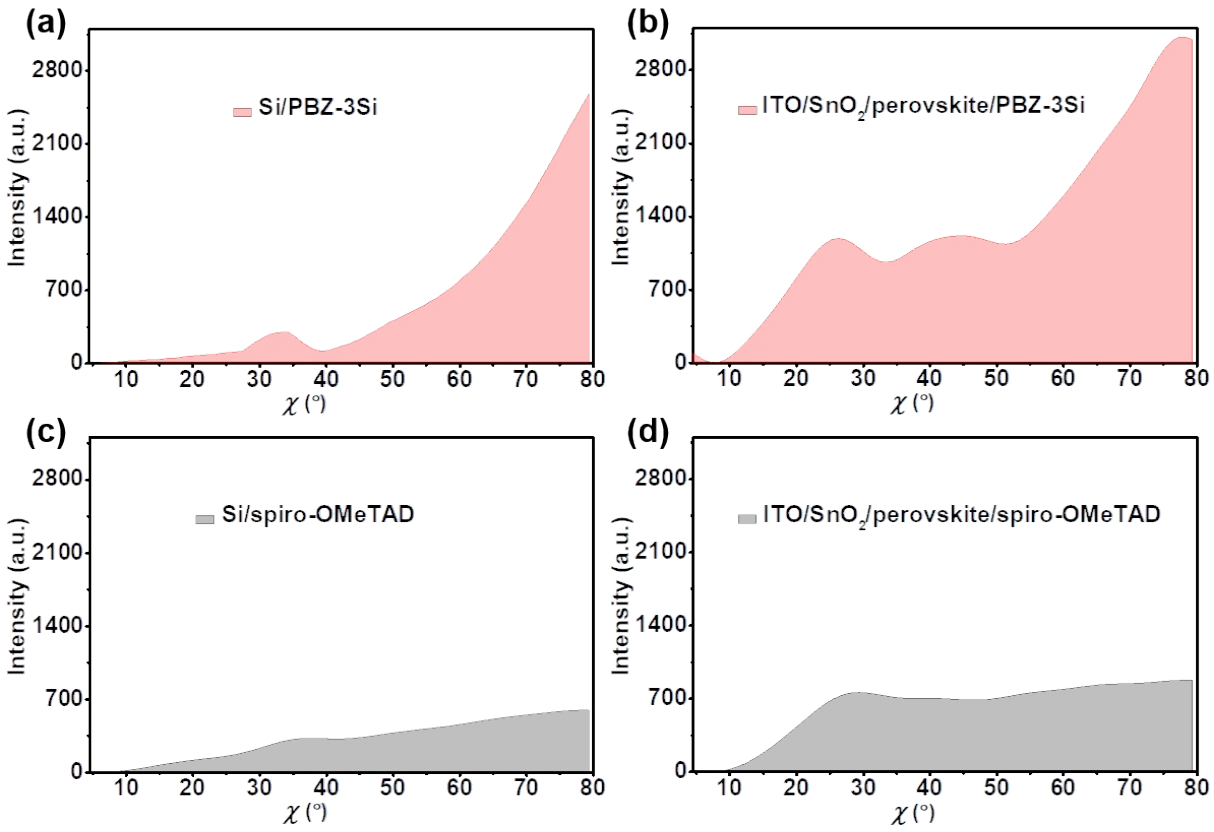

Figure S7. Integration of the azimuthal intensity along the 010 reflex (~1.75 Å $^{-1}$) in GIWAXS for different films.

Table S2. Statistics of all parameters of TRPL.

Samples	τ_1 (ns)	τ_2 (ns)	A_1	A_2	τ_{avg} [a)] (ns)
Perovskite	7.17	483.78	0.04	0.96	483.48
Perovskite/ PBZ-1Si	5.62	26.53	0.64	0.36	20.85
Perovskite/ PBZ-2Si	5.44	58.24	0.40	0.60	55.12
Perovskite/ PBZ-3Si	3.49	81.14	0.58	0.42	76.78

[a)] τ_{avg}: average lifetime which is calculated as following: $\tau_{avg} = (A_1\tau_1^2 + A_2\tau_2^2)/(A_1\tau_1 + A_2\tau_2)$.

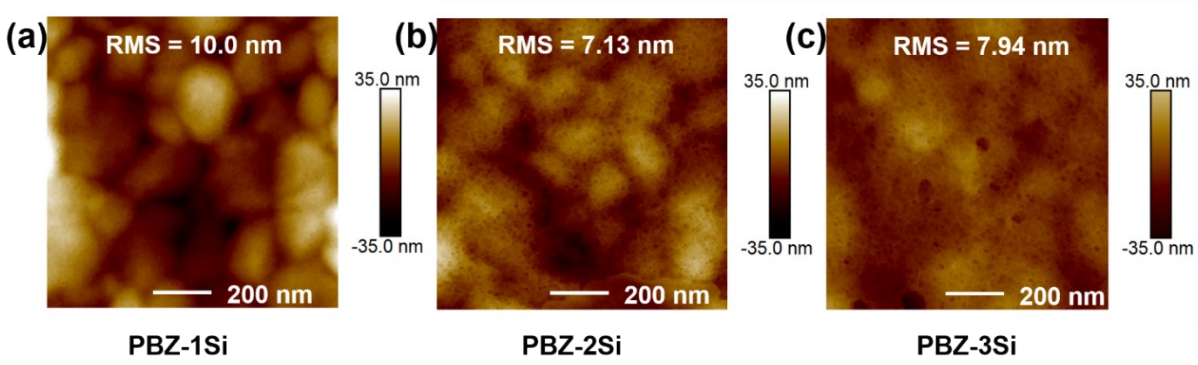

Figure S8. AFM images of PBZ-Si films.

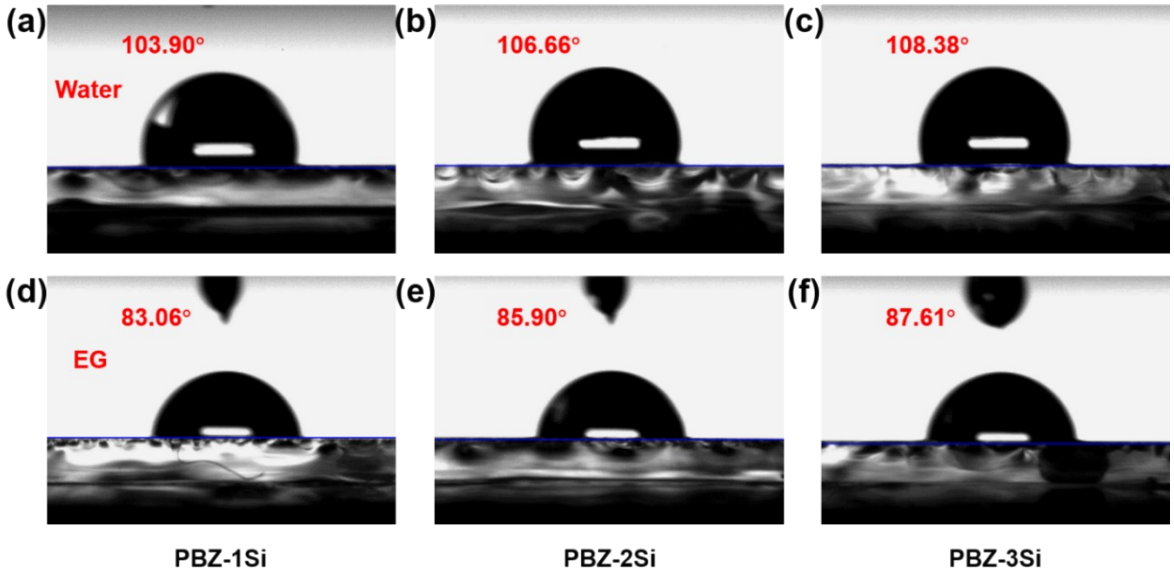

Figure S9. Contact angles (CAs) of water ((a)-(c)) and ethylene glycol (EG) ((d)-(f)) on PBZ-Si films.

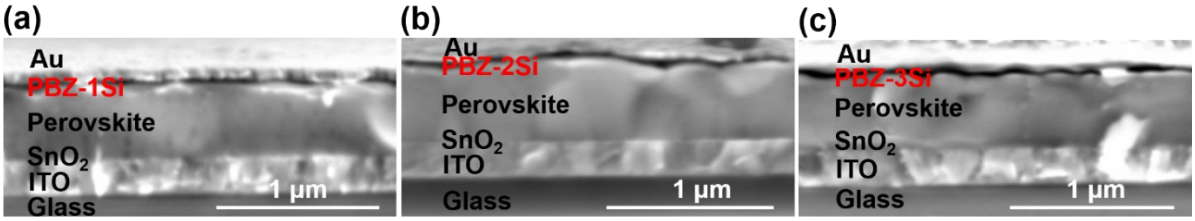

Figure S10. Cross sectional SEM images of the planar n-i-p structured PSCs device with different HTMs, scale bar 1 μm.

Table S3. The *J*–*V* performance of PSCs based on PBZ-1Si HTM films with different precursor concentrations.

Concentration (mg mL^{-1})	V_{OC} (V)	J_{SC} (mA cm^{-2})	FF (%)	PCE (%)
4	1.03	21.37	78.32	17.24
6	1.00	21.15	70.92	15.00
8	1.00	20.47	65.02	13.31

Table S4. The *J*–*V* performance of PSCs based on PBZ-2Si HTM films with different precursor concentrations.

Concentration (mg mL^{-1})	V_{OC} (V)	J_{SC} (mA cm^{-2})	FF (%)	PCE (%)
4	1.05	21.61	74.17	16.83
6	1.06	22.22	81.31	19.15
8	1.04	21.56	71.16	16.00

Table S5. The *J–V* performance of PSCs based on PBZ-3Si HTM films with different precursor concentrations.

Concentration (mg mL^{-1})	V_{OC} (V)	J_{SC} (mA cm^{-2})	FF (%)	PCE (%)
4	1.08	21.43	80.37	18.60
6	1.09	21.80	84.93	20.18
8	1.08	20.79	81.95	18.40

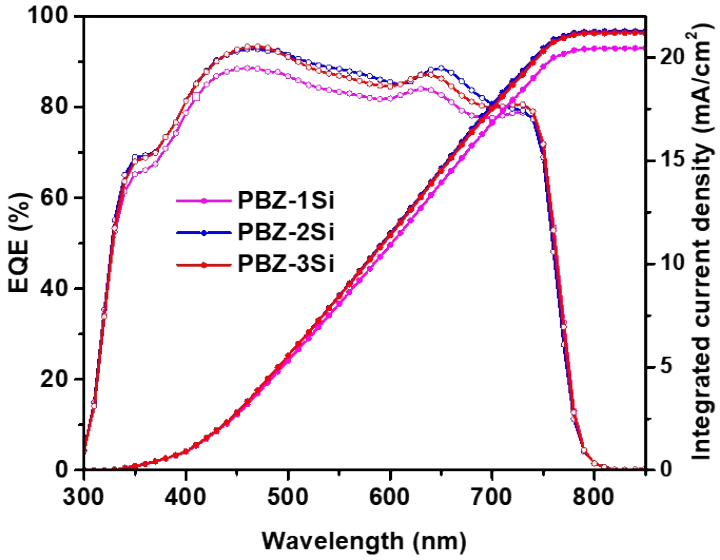

Figure S11. The EQE and the corresponding J_{SC} derived from the PBZ-Si based PSCs.

Table S6. A summary of high FFs and their corresponding efficiencies obtained in various dopant-free HTMs published in recent years and from this work.

HTM	Type	FF (%)	PCE (%)	Device structure	Ref.	Year
P3HT	polymer	82.5	23.2	FTO/SnO_2/$(FAPbI_3)_{0.95}(MAPbBr_3)_{0.05}$(DHA)/HTM/Au	7	2021
P3	polymer	80.0	20.3	FTO/mp-SnO_2/$MAPbI_3$/HTM/Au	8	2019

PCDTBT1	polymer	78.2	19.1	ITO/TiO_2/$PC_{60}BM$/$MAPbI_3$/HTM/MoO_3/Au	9	2018
PTEG	polymer	77.0	19.8	FTO/SnO_2/$CsFAMAPbI_{3-x}Br_x$/HTM/Au	10	2018
PBDTT	polymer	76.67	20.28	ITO/SnO_2/$CsFAMAPbI_{3-x}Br_x$/HTM/MoO_3/Ag	11	2020
alkoxy-PTEG	polymer	79.8	21.2	FTO/SnO_2/$Cs_{0.06}FA_{0.78}MA_{0.16}Pb_{0.94}I_{2.4}Br_{0.48}$/HTM/Au	12	2020
DTB	polymer	69.85	19.68	FTO/c-TiO_2/m-TiO_2/$FA_{0.85}MA_{0.15}PbI_{2.55}Br_{0.45}$/HTM/Au	13	2018
PC3	polymer	80.0	20.8	FTO/mp-SnO_2/$MAPbI_3$(EACl)/HTM/Au	14	2020
PBDT[2F]T	polymer	72.60	17.52	FTO/SnO_2/$MAPbI_3$/HTM/Ag	15	2020
PBDT-N20	polymer	75	18.9	FTO/TiO_2/mp-TiO_2/$(FAPbI_3)_{0.85}(MAPbBr_3)_{0.15}$/HTM/Au	16	2020
2DP-TDB	polymer	79.57	22.17	ITO/SnO_2/$FA_{0.85}MA_{0.15}PbI_3$/HTM/MoO_3/Ag	17	2021
DTB(3% DEG)	polymer	72.2	20.10	FTO/TiO_2/mp-TiO_2/$Cs_{0.05}FA_{0.81}MA_{0.14}PbI_{2.55}Br_{0.45}$/HTM/Au	18	2019
PDCBT	polymer	80.0	21.2	ITO/C_{60}-SAM/SnOx/$PC_{60}BM$/$FA_{0.83}MA_{0.17}Pb_{1.1}Br_{0.50}I_{2.80}$/HTM/Ta-WOx/Au	19	2017
TCTA-BVP	polymer	78.7	18.27	FTO/TiO_2/C_{60}/$MAPbI_3$/HTM/Ag	20	2016
P25NH	polymer	83.2	17.3	ITO/SnO_2/$(MA_{0.8}FA_{0.2})Pb(I_{0.93}Cl_{0.07})_3$/HTM/Ag	21	2020
PBT1-C	polymer	81.22	19.06	FTO/TiO_2/mp-TiO_2/CsFAMA(xGUAPbI_3)/HTM/MoO_3/Ag	22	2019
FBA3	small molecular	79.9	19.27	ITO/C_{60}/$MAPbI_xCl_{3-x}$/HTM/MoO_3/Ag	23	2019
TPA-ANT-TPA	small molecular	79.6	17.5	FTO/TiO_2/mp-TiO_2/$MAPbI_3$/HTM/Ag	24	2018
DTP-C6Th	small molecular	79.9	21.04	FTO/SnO_2/C_{60}-SAM/$MA_{0.7}FA_{0.3}Pb(I_{0.925}Br_{0.075})_3$/PMMA/HTM/Au	25	2019
OMe-TPA-CuPc	organometallic	76.7	19.67	FTO/SnO_2/$Cs_{0.05}(MA_{0.13}FA_{0.87})_{0.95}Pb(I_{0.87}Br_{0.13})_3$/HTM/Au	26	2019
CuSCN	inorganic	78.2	20.4	FTO/TiO_2/mp-TiO_2/$CsFAMAPbI_{3-x}Br_x$/HTM/rGO/Au	27	2017
PBZ-3Si	**polymer**	**84.93**	**20.18**	**ITO/SnO_2/$CsFAMAPbI_{3-x}Br_x$/HTM/Au**	**This work**	

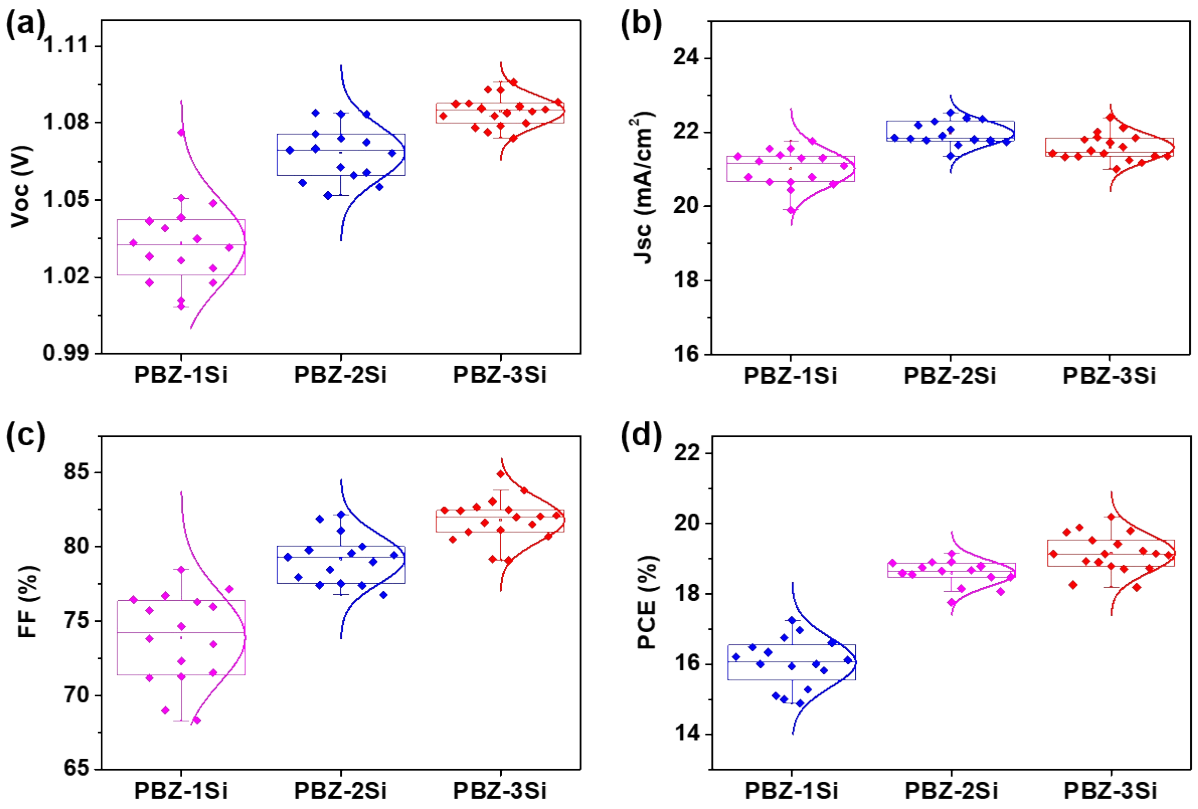

Figure S12. Statistical box plots of the photovoltaic parameters (*Voc, Jsc*, FF, and PCE, respectively) of the devices with different HTMs in the forward scanning direction.

Table S7. Average photovoltaic parameters over 15 devices with different HTMs

HTM	V_{OC} (V)	J_{SC} (mA cm^{-2})	FF (%)	PCE (%)
PBZ-1Si	1.03 ± 0.02	21.02 ± 0.49	73.89 ± 3.04	16.04 ± 0.70
PBZ-2Si	1.07 ± 0.01	21.96 ± 0.32	79.18 ± 1.65	18.58 ± 0.36
PBZ-3Si	1.08 ± 0.01	21.58 ± 0.36	81.80 ± 1.46	19.15 ± 0.54

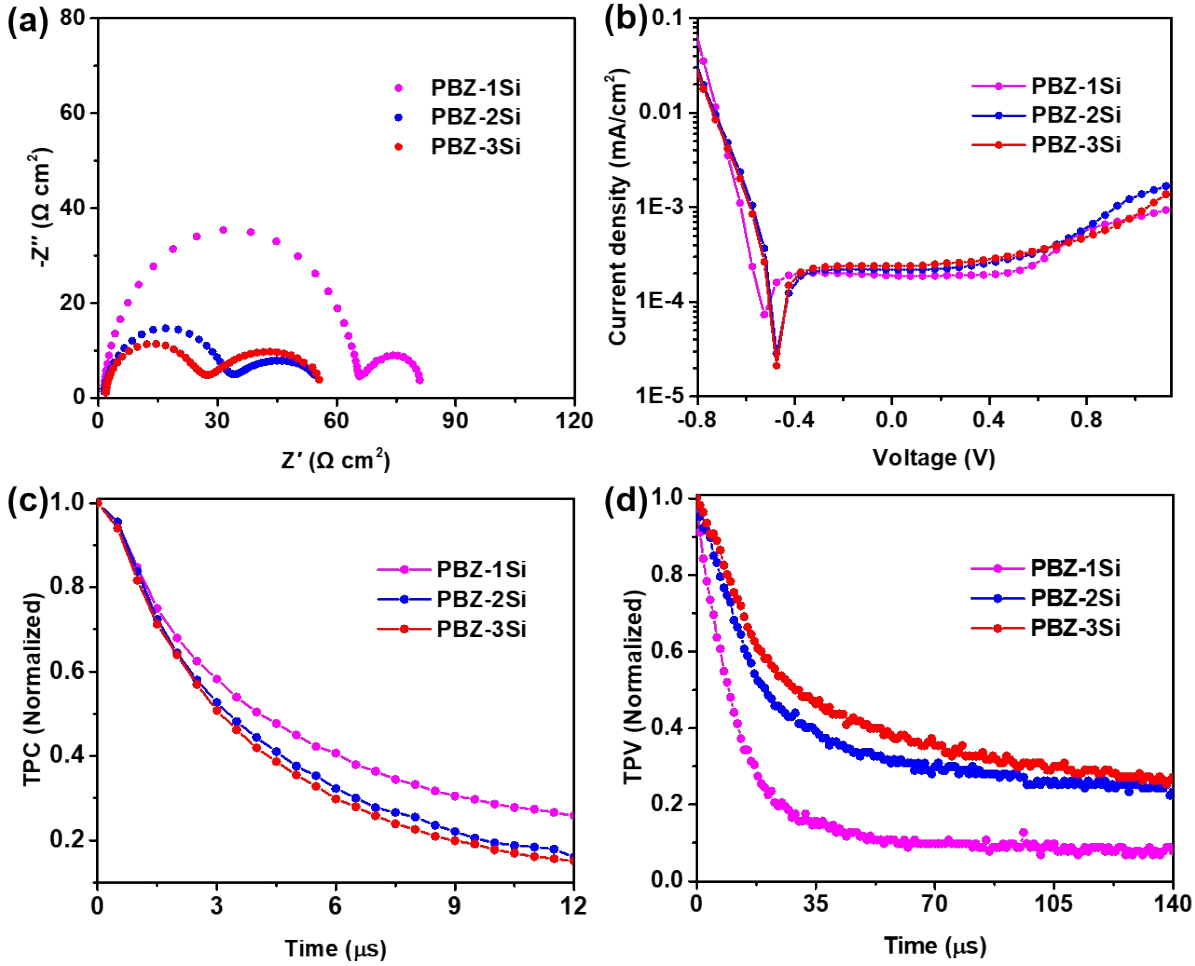

Figure S13. (a) Electrical impedance spectroscopy (EIS), Nyquist plot from the PBZ-Si based devices. (b) Dark *J*–*V* curves for devices based on PBZ-Si. (c) Transient photocurrent decay for devices based on PBZ-Si. (d) Transient photovoltage decay for devices based on PBZ-Si.

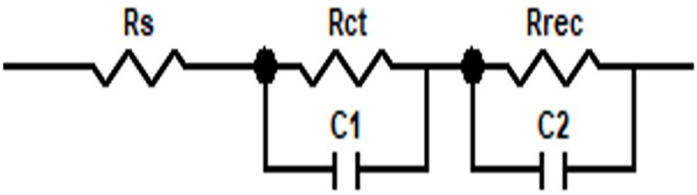

Figure S14. Equivalent circuit model for the Nyquist plots. Rs: series resistance. R_{ct}:transfer/transport resistance. R_{rec}: resistance of interfacial recombination. C: capacitance.

Table S8. EIS derived series resistance (R_s), transport resistance (R_{ct}) and recombination resistance (R_{rec}) for the different devices under 10 mW cm^{-2} illumination at applied voltages (-0.85V).

Samples	R_s (Ω cm^2)	R_{ct} (Ω cm^2)	R_{rec} (Ω cm^2)
PBZ-1Si	1.32	65.16	16.26
PBZ-2Si	1.54	31.37	19.18
PBZ-3Si	1.88	25.18	24.14

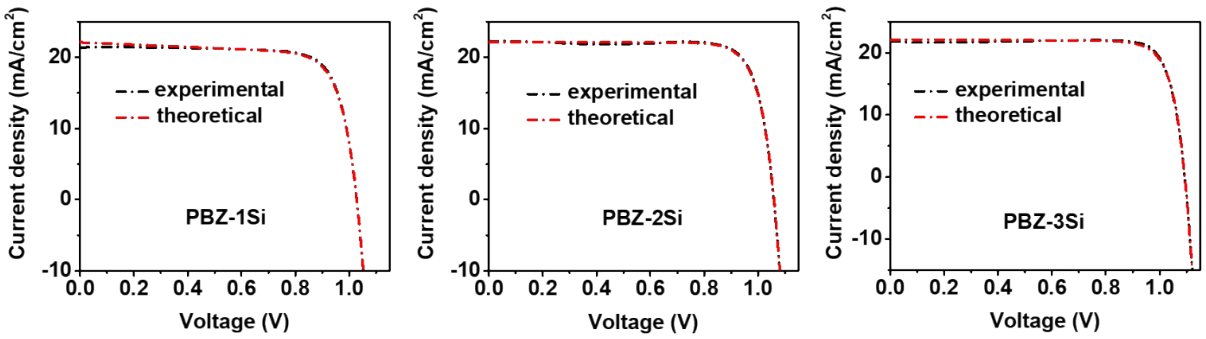

Figure S15. The comparison of *J-V* curves between the theoretical simulation and experimental measurement. Theoretically fitted *J-V* curves by modified detailed balance model and experimentally measured *J-V* characteristics for PBZ-1Si, PBZ-2Si and PBZ-3Si based devices with the champion efficiency, respectively.

Table S9. The parameters retrieved from the *J-V* curves of different cases.

Samples	γ_{bulk} (s^{-1})	U_{surf} (nm cm^3 s^{-1})	R_s (Ω cm^2)	R_{sh} (Ω cm^2)
PBZ-1Si	8.29×10^7	2.90×10^{-6}	7.45	1.15×10^4
PBZ-2Si	4.08×10^7	1.13×10^{-5}	10.38	59.41×10^4
PBZ-3Si	1.53×10^7	6.65×10^{-6}	10.13	9.25×10^4

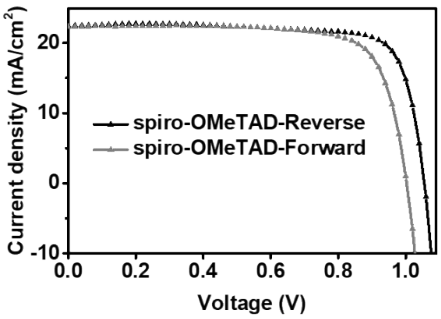

Figure S16. The J–V curves of PSCs with doped spiro-OMeTAD as HTMs. The concentration spiro-OMeTAD is typically 72.3 mg/mL with 17.5 μL of Li-TFSI solution (520 mg mL^{-1}) in acetonitrile and 28.5 μL of TBP as dopants.

Table S10. Photovoltaic parameters of PSCs based on doped spiro-OMeTAD as HTMs

HTM	Scan	V_{OC} (V)	J_{SC} (mA cm^{-2})	FF (%)	PCE (%)
spiro-OMeTAD	Forward	1.00	22.32	76.57	17.09
	Reverse	1.05	22.50	79.53	18.79

References

1 W. S. Yang, B. Park, E. H. Jung, N. J. Jeon, Y. C. Kim, D. U. Lee, S. S. Shin, J. Seo, E. K. Kim, J. H. Noh and S. Il Seok, *Science*, 2017, **356**, 1376–1379.

2 M. Saliba, T. Matsui, J.-Y. Seo, K. Domanski, J.-P. Correa-Baena, M. K. Nazeeruddin, S. M. Zakeeruddin, W. Tress, A. Abate, A. Hagfeldt and M. Grätzel, *Energy & Environmental Science*, 2016, **9**, 1989–1997.

3 D. Li, J.-Y. Shao, Y. Li, Y. Li, L.-Y. Deng, Y.-W. Zhong and Q. Meng, *Chemical Communications*, 2018, **54**, 1651–1654.

4 M. J. Frisch, G. W. Trucks, H. B. Schlegel, G. E. Scuseria, M. A. Robb, J. R. Cheeseman, G. Scalmani, V. Barone, G. A. Petersson, H. Nakatsuji, X. Li, M. Caricato, A. Marenich, J. Bloino, B. G. Janesko, R. Gomperts, B. Mennucci, H. P. Hratchian, J. V. Ortiz, A. F. Izmaylov, J. L. Sonnenberg, D. Williams-Young, F. Ding, F. Lipparini,

F. Egidi, J. Goings, B. Peng, A. Petrone, T. Henderson, D. Ranasinghe, V. G. Zakrzewski, J. Gao, N. Rega, G. Zheng, W. Liang, M. Hada, M. Ehara, K. Toyota, R. Fukuda, J. Hasegawa, M. Ishida, T. Nakajima, Y. Honda, O. Kitao, H. Nakai, T. Vreven, K. Throssell, J. A. Montgomery, Jr., J. E. Peralta, F. Ogliaro, M. Bearpark, J. J. Heyd, E. Brothers, K. N. Kudin, V. N. Staroverov, T. Keith, R. Kobayashi, J. Normand, K. Raghavachari, A. Rendell, J. C. Burant, S. S. Iyengar, J. Tomasi, M. Cossi, J. M. Millam, M. Klene, C. Adamo, R. Cammi, J. W. Ochterski, R. L. Martin, K. Morokuma, O. Farkas, J. B. Foresman, and D. J. Fox, Gaussian, Inc., Wallingford CT, 2016.

5 T. Lu and F. Chen, *Journal of Computational Chemistry*, 2012, **33**, 580–592.

6 H. Bin, Z. G. Zhang, L. Gao, S. Chen, L. Zhong, L. Xue, C. Yang and Y. Li, *Journal of the American Chemical Society*, 2016, **138**, 4657–4664.

7 M. J. Jeong, K. M. Yeom, S. J. Kim, E. H. Jung and J. H. Noh, *Energy & Environmental Science*, 2021, **14**, 2419–2428.

8 F. Zhang, Z. Yao, Y. Guo, Y. Li, J. Bergstrand, C. J. Brett, B. Cai, A. Hajian, Y. Guo, X. Yang, J. M. Gardner, J. Widengren, S. V. Roth, L. Kloo and L. Sun, *Journal of the American Chemical Society*, 2020, **141**, 19700–19707.

9 F. Cai, J. Cai, L. Yang, W. Li, R. S. Gurney, H. Yi, A. Iraqi, D. Liu and T. Wang, *Nano Energy*, 2018, **45**, 28–36.

10 G.-W. Kim, J. Lee, G. Kang, T. Kim and T. Park, *Advanced Energy Materials*, 2018, **8**, 1701935.

11 G. You, Q. Zhuang, L. Wang, X. Lin, D. Zou, Z. Lin, H. Zhen, W. Zhuang and Q. Ling, *Advanced Energy Materials*, 2020, **10**, 1903146.

12 J. Lee, G. Kim, M. Kim, S. A. Park and T. Park, *Advanced Energy Materials*, 2020, **10**, 1902662.

13 L. Zhang, C. Liu, J. Zhang, X. Li, C. Cheng, Y. Tian, A. K.-Y. Jen and B. Xu, *Advanced Materials*, 2018, **30**, 1804028.

14 Z. Yao, F. Zhang, Y. Guo, H. Wu, L. He, Z. Liu, B. Cai, Y. Guo, C. J. Brett, Y. Li, C. V. Srambickal, X. Yang, G. Chen, J. Widengren, D. Liu, J. M. Gardner, L. Kloo and L. Sun, *Journal of the American Chemical Society*, 2020, **142**, 17681–17692.

15 X. Kong, Y. Jiang, X. Wu, C. Chen, J. Guo, S. Liu, X. Gao, G. Zhou, J.-M. Liu, K. Kempa and J. Gao, *Journal of Materials Chemistry A*, 2020, **8**, 1858–1864.

16 X. Jiang, X. Liu, J. Zhang, S. Ahmad, D. Tu, W. Qin, T. Jiu, S. Pang, X. Guo and C. Li, *Journal of Materials Chemistry A*, 2020, **8**, 21036–21043.

17 Q. Fu, Z. Xu, X. Tang, T. Liu, X. Dong, X. Zhang, N. Zheng, Z. Xie and Y. Liu, *ACS Energy Letters*, 2021, 1521–1532.

18 L. Zhang, C. Liu, X. Wang, Y. Tian, A. K. Y. Jen and B. Xu, *Advanced Functional Materials*, 2019, **29**, 1904856.

19 Y. Hou, X. Du, S. Scheiner, D. P. McMeekin, Z. Wang, N. Li, M. S. Killian, H. Chen, M. Richter, I. Levchuk, N. Schrenker, E. Spiecker, T. Stubhan, N. A. Luechinger, A. Hirsch, P. Schmuki, H.-P. Steinrück, R. H. Fink, M. Halik, H. J. Snaith and C. J. Brabec, *Science*, 2017, **358**, 1192–1197.

20 Z. Li, Z. Zhu, C.-C. Chueh, J. Luo and A. K.-Y. Jen, *Advanced Energy Materials*, 2016, **6**, 1601165.

21 W. Liu, Y. Ma, Z. Wang, M. Zhu, J. Wang, M. Khalil, H. Wang, W. Gao, W. J. Fan, W.-S. Li and Q. Zhang, *ACS Applied Energy Materials*, 2020, **3**, 9600–9609.

22 F. Qi, X. Deng, X. Wu, L. Huo, Y. Xiao, X. Lu, Z. Zhu and A. K. Y. K. -Y. Jen, *Advanced Energy Materials*, 2019, **9**, 1902600.

23 X. Sun, F. Wu, C. Zhong, L. Zhu and Z. Li, *Chemical Science*, 2019, **10**, 6899–6907.

24 H. D. Pham, T. T. Do, J. Kim, C. Charbonneau, S. Manzhos, K. Feron, W. C. Tsoi, J. R. Durrant, S. M. Jain and P. Sonar, *Advanced Energy Materials*, 2018, **8**, 1703007.

25 X. Yin, J. Zhou, Z. Song, Z. Dong, Q. Bao, N. Shrestha, S. S. Bista, R. J. Ellingson, Y. Yan and W. Tang, *Advanced Functional Materials*, 2019, **29**, 1904300.

26 Y. Feng, Q. Hu, E. Rezaee, M. Li, Z. Xu, A. Lorenzoni, F. Mercuri and M. Muccini, *Advanced Energy Materials*, 2019, 1901019.

27 N. Arora, M. I. Dar, A. Hinderhofer, N. Pellet, F. Schreiber, S. M. Zakeeruddin and M. Grätzel, *Science*, 2017, **358**, 768–771.